Sparse Multichannel Decomposition of Electrodermal Activity With Physiological Priors

Samiul Alam [iD], Md. Rafiul Amin [iD], *Student Member, IEEE*, and Rose T. Faghih [iD], *Senior Member, IEEE*

Abstract—*Goal:* Inferring autonomous nervous system (ANS) activity is a challenging issue and has critical applications in stress regulation. Sweat secretions caused by ANS activity influence the electrical conductance of the skin. Therefore, the variations in skin conductance (SC) measurements reflect the sudomotor nerve activity (SMNA) and can be used to infer the underlying ANS activity. These variations are strongly correlated with emotional arousal as well as thermoregulation. However, accurately recovering ANS activity and the corresponding state-space system from a single channel signal is difficult due to artifacts introduced by measurement noise. To minimize the impact of noise on inferring ANS activity, we utilize multiple channels of SC data. *Methods:* We model skin conductance using a second-order differential equation incorporating a time-shifted sparse impulse train input in combination with independent cubic basis spline functions. Finally, we develop a block coordinate descent method for SC signal decomposition by employing a generalized cross-validation sparse recovery approach while including physiological priors. *Results:* We analyze the experimental data to validate the performance of the proposed algorithm. We demonstrate its capacity to recover the ANS activations, the underlying physiological system parameters, and both tonic and phasic components. Finally, we present an overview of the algorithm's comparative performance under varying conditions and configurations to substantiate its ability to accurately model ANS activity. Our results show that our algorithm performs better in terms of multiple metrics like noise performance, AUC score, the goodness of fit of reconstructed signal, and lower missing impulses compared with the single channel decomposition approach. *Conclusion:* In this study, we highlight the challenges and benefits of concurrent decomposition and deconvolution of multichannel SC signals.

Index Terms—Biomedical Signal Processing, optimization, multichannel Deconvolution, system Identification, sparse Recovery.

Impact Statement—Multichannel decomposition of electrodermal activity enables more robust inference of ANS activity from noisy SC data in real-world settings to then obtain insights into a person's mental well-being.

I. INTRODUCTION

ELECTRODERMAL activity (EDA) is a measure of neurally mediated effects on sweat gland permeability, observed as changes in skin conductance (SC) [1]. EDA is influenced by the body's thermoregulation system, primarily controlled by the hypothalamic area [2]. However, it can also represent the effects of other physiological events including emotional arousal [3] originating from the autonomous nervous system (ANS). We can therefore observe these variations to infer important characteristics of ANS activity. Additionally, SC measurement is quite trivial and can be incorporated into wearables like smart gloves and watches [4], [5], [6]. Such devices can be used to track the mental health and well-being of users. Hence, an additional understanding of EDA and how it correlates with ANS activity is essential.

Skin conductance signal consists of two components - phasic and tonic [7], [8], [9], [10], [11]. The tonic component of the signal is a slowly varying wave, whereas the phasic component is fast varying. It has been shown in [7], [12] that the tonic component is mainly related to the thermoregulation of the body. The phasic component, however, is related to the neural activity of the brain. Changes in mental states like frustration, anger, and fear can cause the skin in different parts of the body to secrete sweat and as a result, cause changes in SC. Information related to ANS activity is encoded in the phasic component of the signal, and it has been shown in [13] that the information contained in the phasic component can be used to track the ANS activity.

Measuring skin conductance (SC) data is noninvasive and cost-effective. The ability to use SC data for monitoring arousal

has significant applications and has been historically employed in psychological research [14]. The SC signal encompasses a wealth of physiological information related to arousal, making it valuable for tracking mental health and well-being [15], [16], [17]. In conjunction with wearable smart devices, SC data can alert patients, friends, family members, or nearby individuals. Such devices have the potential to prevent and alleviate mental breakdowns [18], [19], [20], [21]. Increased stress and pain levels are associated with a higher risk of suicide, as noted in [22]. Therefore, investigating the feasibility of utilizing SC signals to effectively track emotional distress on a daily basis is warranted. Additionally, SC data can be employed to monitor and regulate stress in workplaces, potentially enhancing productivity. Electrodermal activity (EDA) has been used alongside other physiological sensors to monitor workplace stress, as demonstrated in a case study in [23]. Improved stress regulation could boost employee productivity and benefit mental health. The extraction of reliable arousal state information from Skin Conductance (SC) signals calls for the effective separation of tonic and phasic components, a process crucial to understanding distinct physiological stimuli [8]. Previous studies [10], [11], [24], [25], [26], [27], [28], [29], [30], [31], [32], [33], [34], [35], [36], [37], [38] have made strides towards this goal, predominantly employing single-channel data. This study innovates by applying a multi-channel approach, concurrently separating tonic and phasic components from SC data, using physiological priors as an inherent part of the optimization problem. This approach is designed to avoid the pitfalls of fixed SCR shape parameters, which can hamper accuracy, and overfitting, which is a common issue in model design. We assume that SCR shape parameters are Gaussian distributed and utilize this as a prior, informed by parameter estimates from previous research [35], [39]. The result is an enhancement in the accuracy of system identification, leading to a deeper understanding of the physiological processes governing SC responses and ANS activity. Our work paves the way for further advancements in real-time SC data analysis. To recover ANS activity, previous works relied on modeling the system as a second-order differential equation [8], [26], [34], [35]. The model is grounded in the diffusion and evaporation processes of sweat, which connect SC to unknown ANS activity. The main challenge lies in optimization, as the equations become non-convex. This issue is addressed through a systematic approach combining sparse recovery with generalized cross-validation. The optimization is particularly challenging due to the presence of high noise levels, which often render noisy signals difficult to deconvolve effectively and necessitate their exclusion. Concurrent multi-channel deconvolution can overcome the challenges of noise by using multiple channels to accurately estimate essential system parameters for signal recovery. Estimating ANS activity from multiple channels may lead to a more robust approach resistant to noise, as shown in [35]. However, this method does not concurrently decompose the tonic component; instead, it removes it from each channel separately first, resulting in information loss that could be useful for parameter estimation during optimization. Concurrent decomposition has the potential to enhance algorithm stability in situations where noise corruption is present. Such corruption

may arise when electrodes are improperly attached or when considerable movement occurs in close proximity to the electrodes, a scenario observed in related fields such as cardiography [40]. Some channels may also yield irregular or missing impulses due to health issues such as peripheral neuropathy [41], [42]; using multiple channels can aid in recovering all impulses in the response.

Amin et al. [35] also assume that the rise and decay times of impulses in each channel are identical. However, the two durations are correlated but may vary between channels (See Fig. 8). Therefore, employing a concurrent multichannel approach could lead to improved estimation of such parameters [43], [44].

Another challenging aspect of deconvolution is the limited availability of SC data, which typically originates from a small number of patients under laboratory conditions [9], [45], [46]. For real-world deployment, algorithms need to be both efficient and robust. Human skin conductance exhibits non-linearity [47], [48], necessitating a robust model. State-of-the-art models for nonlinear time series data often involve deep learning models, which possess a high degree of freedom and can deliver accurate and robust results. Moreover, their parallelism can be leveraged for acceleration. However, these models can overfit easily due to the large number of parameters involved. To mitigate this issue, a substantial amount of training and evaluation data is required. The data demands for wearable devices measuring SC are particularly high, as users may need to wear them for extended periods and across a wide range of activities. Collecting such data is challenging since SC sensors are not commonly found in consumer-level wearable devices. Consequently, algorithms must be exceptionally robust against noise and over-fitting issues.

In this research, we propose an approach that concurrently decomposes phasic and tonic components within a single state-space model, as demonstrated in [39], but for multichannel observations, as conducted in [35]. We validate our results by comparing the phasic and tonic components to corresponding arousal events and the actual timing of stimulus input.

II. METHODS

A. PsPM-SCRV10 (SCRV) Dataset [49]

SCRV dataset contains SC responses of participants to loud sounds. It has measurements recorded from 3 locations for 26 healthy unmedicated participants (12 males and 14 females) in response to single white noise bursts of 1 s duration and 10 ms ramp (≈ 85 dB). Participants are asked to press a foot pedal upon hearing a stimulus. A detailed description of the experimental setting is given in [49].

Skin conductances were recorded from the following places:
- Thenar/hypothenar of the nondominant hand (Channel 1)
- Volar middle phalanx of the dominant 2nd/3 rd finger (Channel 2)
- Medial plantar surface of the nondominant foot (Channel 3)

Besides this, the study also recorded heartbeat time stamps (channel 5) and respiration (channel 6). The SCRV dataset has

event timings for the auditory stimulation events and is used in this research to investigate the efficacy of the algorithm.

B. Model Formulation

Following the work in [7], we represent the SC signal for a single channel as a combination of the tonic and phasic components as follows,

$$y(t) = y_s(t) + y_p(t) + v(t). \tag{1}$$

where $y(t)$ is the SC signal represented as the sum of the phasic component $y_p(t)$, the tonic component $y_s(t)$, and the noise $v(t)$. We will model the skin conductance following [34] and then extend it to multichannel SC data. These are modeled as follows:

1) Phasic Component: The phasic component can be modeled as a smoothed version of the neural activity. This smoothing is a result of different physiological systems which include the sweat glands, epidermis, blood, and other components. We model this system as the first-order kinetics of diffusion of sweat from the sweat glands to the strata cornea and the evaporation of sweat from the strata cornea [7]. Combining these processes, we get a second-order differential equation given by

$$\tau_d \tau_r \frac{d^2 y_p(t)}{dt^2} + (\tau_d + \tau_r)\frac{dy_p(t)}{dt} + y_p(t) = u(t). \tag{2}$$

where τ_r and τ_d are the rise and fall times, respectively, of the SC response assumed to be constant for the entire duration of the experiment following the assumption made in previous studies [9], [10], [11], [24], [27]. $u(t)$ is defined as a summation of N weighted and shifted impulse functions. This is given as,

$$u(t) = \sum_{i=0}^{N-1} u_i \delta(t - \Delta_i). \tag{3}$$

Δ_i is defined as $\Delta_i = iT_u$ where T_u is the sampling interval of $u(t)$. N is the number of samples in the discrete form of u_t. Since the number of ANS activations is very small compared to the number of samples in the recorded SC signal, we can represent the ANS activations as a sparse vector in the discrete domain for our analysis [27]. We solve the differential equation assuming the sweat duct is empty at time $t = 0$ following previous studies [8], [11], [24], [26], [27]. Hence, the solution to the differential equation becomes,

$$y_p(t) = y_p(0) \exp\left(\frac{t}{\tau_d}\right) + h_\tau(t) * u(t). \tag{4}$$

Here,

$$h_\tau(t) = \begin{cases} \frac{\exp\left(\frac{-t}{\tau_r}\right) - \exp\left(\frac{-t}{\tau_r}\right)}{\tau_r - \tau_d} & t \geq 0 \\ 0 & \text{otherwise} \end{cases}. \tag{5}$$

2) Tonic Component: The tonic component, $y_s(t)$ is modeled as a series of shifted and weighted cubic B spline functions as has been done in [27]. The equation is given as:

$$y_s(t) = \psi(t) * q(t). \tag{6}$$

where,

$$q(t) = \sum_{i=0}^{p-1} q_i(t)\delta(t - (i-1)\kappa_i). \tag{7}$$

Here, P indicates the number of different shifted and scaled cubic B-spline waves used and κ_i is the knot size of the cubic B-spline function. It is related to the smoothness of the tonic component.

3) Extension to Multichannel Data: Since the system responses in various locations in the body can be different (See Fig. 8), we need to add different values for the decay and rise times for each channel. These should give intuitively better results for the deconvolved signal. The (2) for M channels becomes:

$$\tau_{d_1} \tau_{r_1} \frac{d^2 y_{p,1}(t)}{dt^2} + (\tau_{d_1} + \tau_{r_1})\frac{dy_{p,1}(t)}{dt} + y_{p,1}(t) = u(t),$$

$$\tau_{d_2} \tau_{r_2} \frac{d^2 y_{p,2}(t)}{dt^2} + (\tau_{d_2} + \tau_{r_2})\frac{dy_{p,2}(t)}{dt} + y_{p,2}(t) = u(t - \beta_2),$$

$$\vdots$$

$$\tau_{d_M} \tau_{r_M} \frac{d^2 y_{p,M}(t)}{dt^2} + (\tau_{d_M} + \tau_{r_M})\frac{dy_{p,M}(t)}{dt}$$
$$+ y_{p,M}(t) = u(t - \beta_M). \tag{8}$$

Here, β_m is the delay of SNS signals for the mth channel with respect to the 1st channel. Thus, β_1 is 0.

The equations (4) and (6) represent a continuous form system. However, we need to express this as a discrete model to use with discrete data. Let us consider that the SC data is sampled with a period of T_s for N measurements. Let us consider that $x_{2m-1}(t)$ and $x_{2m}(t)$ are the internal states. Then, following [1], [8], [26], [27], the differential equation in the mth channel can be written in a state-space form as:

$$\dot{x}_{2m-1}(t) = -\frac{1}{\tau_{r_m}} x_{2m-1}(t) + \frac{1}{\tau_{r_m}} x_{2m-1}(t), \tag{9}$$

$$\dot{x}_{2m}(t) = -\frac{1}{\tau_{d_m}} x_{2m-1}(t) + \frac{1}{\tau_{d_m}} x_{2m}(t). \tag{10}$$

This corresponds to the continuous equation given by

$$y_m(t) = \alpha_m x_{2m}(t) + \nu_m(t). \tag{11}$$

Here, $y_m(t)$ is the continuous observation variable and $\nu_m(t)$ refers to the noise process. In matrix form, the state-space model can be written as follows:

$$\begin{bmatrix} \dot{x}_{2m-1}(t) \\ \dot{x}_{2m}(t) \end{bmatrix} = \begin{bmatrix} -\frac{1}{\tau_{r_m}} & 0 \\ \frac{1}{\tau_{d_m}} & -\frac{1}{\tau_{d_m}} \end{bmatrix} \begin{bmatrix} x_{2m-1}(t) \\ x_{2m}(t) \end{bmatrix} + \begin{bmatrix} \frac{1}{\tau_{r_m}} \\ 0 \end{bmatrix} u(t), \tag{12}$$

$$y_m(t) = \begin{bmatrix} 0 & \alpha_m \end{bmatrix} \begin{bmatrix} x_{2m-1}(t) \\ x_{2m}(t) \end{bmatrix} + \nu_m(t). \tag{13}$$

In state-space form, the equations become:

$$\dot{\boldsymbol{x}}(t) = \boldsymbol{A_c}\boldsymbol{x}(t) + \boldsymbol{B_c}u(t), \tag{14}$$

$$y(t) = \boldsymbol{C_c}\boldsymbol{x}(t) + \boldsymbol{\nu}(t). \tag{15}$$
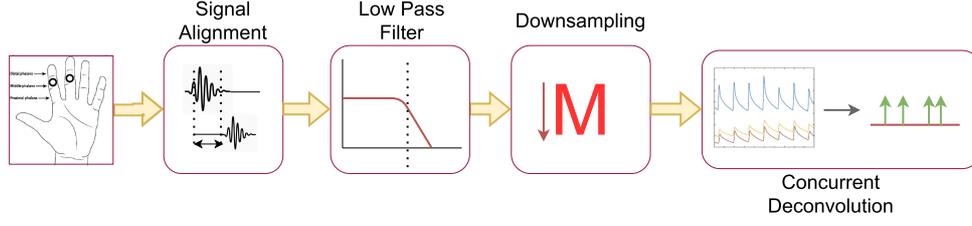
Fig. 1. Preprocessing pipeline for deconvolution Each SC signal passes through a noise calculation block which passes the estimated noise to the deconvolution algorithm. The SC Signals are then aligned, filtered, and downsampled before being fed to the main algorithm block.

Here,

$$\boldsymbol{x}(t) = \begin{bmatrix} x_1(t) \; x_2(t) \; \ldots \; x_{2N}(t) \end{bmatrix}^T_{2N \times 1}$$

$$\boldsymbol{y}(t) = \begin{bmatrix} y_1(t) \; y_2(t) \; \ldots \; y_N(t) \end{bmatrix}^T_{N \times 1}$$

$$\boldsymbol{\nu}(t) = \begin{bmatrix} \nu_1(t) \; \nu_2(t) \; \vdots \; \nu_N(t) \end{bmatrix}^T_{N \times 1} \quad \boldsymbol{A_c}$$

$$= \begin{bmatrix} \boldsymbol{a}_1 & 0 & \ldots & 0 \\ 0 & \boldsymbol{a}_2 & \ldots & 0 \\ \vdots & 0 & \ddots & \vdots \\ 0 & 0 & \ldots & \boldsymbol{a}_N \end{bmatrix}_{2N \times 2N}$$

where,

$$\boldsymbol{a}_n = \begin{bmatrix} -\frac{1}{\tau_{rn}} & 0 \\ \frac{1}{\tau_{dn}} & -\frac{1}{\tau_{dn}} \end{bmatrix},$$

$$\boldsymbol{B_c} = \begin{bmatrix} \boldsymbol{b}_1 & \boldsymbol{b}_2 \ldots \boldsymbol{b}_N \end{bmatrix}_{2N \times 1},$$

where

$$b_n = \begin{bmatrix} \frac{1}{\tau_{rn}} & 0 \end{bmatrix},$$

and

$$C_c = \begin{bmatrix} \boldsymbol{c}_1 & 0 & \ldots & 0 \\ 0 & \boldsymbol{c}_2 & \ldots & 0 \\ \vdots & 0 & \ddots & \vdots \\ 0 & 0 & \ldots & \boldsymbol{c}_N \end{bmatrix}_{2N \times 2N}$$

where,

$$c_n = \begin{bmatrix} 0 & 1 & 0 & 0 \\ 0 & 1 & 0 & \alpha_n \end{bmatrix}$$

4) Discretization: Let $T_u = 0.25$ s and $T_y = 1$ s be the sampling interval of ANS activity and the phasic SC data, respectively, for each channel. The timing of the neural impulses can be written as $\gamma_i = iT_u$; u_i is zero if there is no impulse at the ith instance. Let $y_{m,k}$ be the observed phasic SC for the mth channel at time instance $t_k = kT_y$. We can write

$$y_{m,k} = \alpha_m x_{2m}(t_k) + \nu_{m,k}. \tag{16}$$

where $\nu_{m,k}$ is the noise associated with the mth channel; $\nu_{m,k}$ is a zero-mean Gaussian random variable. Under the

assumption that the input and states are constant over T_u, the discrete form of the ANS activations can be written as a vector $\boldsymbol{u} = \begin{bmatrix} u_1 & u_2 & \cdots & u_L \end{bmatrix}^\top$ that represents the ANS activity over the entire duration of SC data. Let $\Phi = e^{A_c T_u}$, and $\Gamma = \int_0^{T_u} e^{A_c(T_u - \rho)} B_c d\rho$. Then we can write the discrete state-space equivalent of (14)–(15)) as:

$$\boldsymbol{x}[k+1] = \Phi \boldsymbol{x}[k] + \Gamma \boldsymbol{u}[k], \tag{17}$$

$$\boldsymbol{y}[k] = C_c \boldsymbol{x}[k] + \boldsymbol{\nu}[k]. \tag{18}$$

Since, $T_u \neq T_y$, let, $T_y = LT_u$ where L is a positive integer, we let

$$A_d = \Phi^L,$$

$$B_d = \begin{bmatrix} \Phi^{L-1}\Gamma & \Phi^{L-2}\Gamma & \cdots & \Gamma \end{bmatrix},$$

$$\boldsymbol{u}_d[k] = \begin{bmatrix} \boldsymbol{u}[Lk] & \boldsymbol{u}[Lk+1] & \cdots & \boldsymbol{u}[Lk+L-1] \end{bmatrix}^\top,$$

$$\nu_d[k] = \nu[Lk] \text{ and } \boldsymbol{z}[k] = \boldsymbol{x}[Lk];$$

Thus, the multi-rate system can be represented as follows:

$$\boldsymbol{z}[k+1] = A_d \boldsymbol{z}[k] + B_d \boldsymbol{u}_d[k], \tag{19}$$

$$\boldsymbol{y}[k] = C_c \boldsymbol{z}[k] + \nu_d[k]. \tag{20}$$

where A_d and B_d are functions of $\boldsymbol{\tau} = \begin{bmatrix} \tau_r & \tau_d \end{bmatrix}^\top$, $\boldsymbol{\alpha}$, T_u, and T_y. Let $\boldsymbol{\theta} = \begin{bmatrix} \boldsymbol{\tau}^\top & \boldsymbol{\alpha}^\top \end{bmatrix}^\top$. Since the system is causal, we use (19)–(20) to obtain the observation equation for the kth sample:

$$\boldsymbol{y}[k] = \mathcal{F}[k] \boldsymbol{z}[0] + \mathcal{D}[k] \boldsymbol{u} + \boldsymbol{\nu}_d[k]. $$

where $\mathcal{F}[k] = C_c A_d^k$,

$$\mathcal{D}[k] = C_c [A_d^{k-1} B_d \; A_d^{k-2} B_d \; \cdots \; B_d \underbrace{0 \; \cdots \; 0}_{N-kL}],$$

and $\boldsymbol{u} = \begin{bmatrix} \boldsymbol{u}_d[0] & \boldsymbol{u}_d[1] & \cdots & \boldsymbol{u}_d[k-1] & \cdots & \boldsymbol{u}_d[M-1] \end{bmatrix}^\top_{N \times 1}$. For the initial condition, we can let $\boldsymbol{z}_{\theta_0} = \boldsymbol{z}[0] = \begin{bmatrix} 0 \; y_1(0) \; 0 \; \frac{y_2(0)}{\alpha_2} \; \cdots \; 0 \; \frac{y_M(0)}{\alpha_M} \end{bmatrix}^\top$ similar to the work in [26].

Then, let $\boldsymbol{y} = \begin{bmatrix} \boldsymbol{y}[1]^\top & \boldsymbol{y}[2]^\top & \cdots & \boldsymbol{y}[N]^\top \end{bmatrix}^\top_{MN \times 1}$ where $\boldsymbol{y}[k] = \begin{bmatrix} \boldsymbol{y}_{1,k} & \boldsymbol{y}_{2,k} & \cdots & \boldsymbol{y}_{M,k} \end{bmatrix}^\top$, $\forall k \in \{1, 2, \ldots, M\}$. Similarly, $\boldsymbol{\nu} = \begin{bmatrix} \nu_d[1] & \nu_d[2] & \cdots & \nu_d[N] \end{bmatrix}^\top_{MN \times 1}$ where $\boldsymbol{\nu}_d[k] = \begin{bmatrix} \boldsymbol{\nu}_{1,k} & \boldsymbol{\nu}_{2,k} & \cdots & \boldsymbol{\nu}_{M,k} \end{bmatrix}^\top$, $\forall k \in \{1, 2, \ldots, N\}$. Moreover, let $\mathcal{F}_{\boldsymbol{\theta}} = \begin{bmatrix} \mathcal{F}[0] & \mathcal{F}[1] & \cdots & \mathcal{F}[N-1] \end{bmatrix}^\top_{MN \times 2M}$ and $\mathcal{D}_{\boldsymbol{\theta}} = \begin{bmatrix} \mathcal{D}[0] & \mathcal{D}[1] & \cdots & \mathcal{D}[N-1] \end{bmatrix}^\top_{MN \times L}$. Therefore, we can write the solution for the observation equation for all the sampled data as
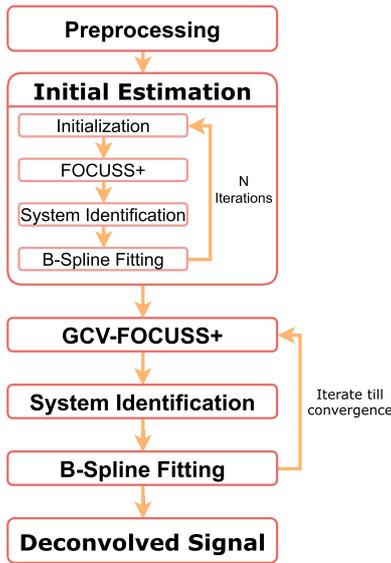
Fig. 2. Simplified overview of our algorithm. The algorithm has two stages to aid convergence - one for initial estimation and the next for fine-tuning output.

follows,

$$y = \mathcal{F}_{\boldsymbol{\theta}} z_{\boldsymbol{\theta}_0} + \mathcal{D}_{\boldsymbol{\theta}} u + \nu.$$

Equivalently, we can separately represent the solution for each channel as follows:

$$y_1 = \mathcal{F}_{\boldsymbol{\theta}_1} z_{\boldsymbol{\theta}_0} + \mathcal{D}_{\boldsymbol{\theta}_1} u + \nu_1,$$

$$y_2 = \mathcal{F}_{\boldsymbol{\theta}_2} z_{\boldsymbol{\theta}_0} + \mathcal{D}_{\boldsymbol{\theta}_2} u + \nu_2,$$

$$\vdots$$

$$y_N = \mathcal{F}_{\boldsymbol{\theta}_N} z_{\boldsymbol{\theta}_0} + \mathcal{D}_{\boldsymbol{\theta}_N} u + \nu_2. \quad (21)$$

Here $y_n, \mathcal{F}_{\boldsymbol{\theta}_n}, \mathcal{D}_{\boldsymbol{\theta}_n}$, and ν_n correspond to the vector and matrices taking the $(N(k-1)+n)^{th}$ rows from $y, \mathcal{F}_{\boldsymbol{\theta}}, \mathcal{D}_{\boldsymbol{\theta}}$, and ν, respectively, $\forall k \in \{1, 2, 3, \ldots, M\}$.

For each channel, we independently obtain the tonic component from (6). Let $\boldsymbol{q}_m$ be the weights and G_m be the coefficients of the b-spline functions for the mth channel. These are independent of each other and therefore the tonic component for the mth channel is given by

$$y_{s_m} = G_m \boldsymbol{q}_m. \quad (22)$$

For ease of notation, we combine all model parameters to obtain $\boldsymbol{\theta} = \left[\tau^T, z_{\boldsymbol{\theta}_0}^T, \boldsymbol{\alpha}^T \right]$.

C. Estimation

A brief overall flowchart of the algorithm is presented in Fig. 2. The estimation occurs in two stages. We pre-process the signal and for a fixed number of iterations (N_{init}), we use a sparse recovery algorithm to get an initial estimate of ANS activity. This algorithm is called FOcal Underdetermined System Solver (FOCUSS+) and allows for solving for non-negative sparse inputs [50]. We use this estimate to update system parameters and the cubic B-spline coefficients. Next, we

iterate with a more accurate sparse recovery algorithm. In our case, we use an algorithm known as GCV-FOCUSS+, which combines FOCUSS+ and generalized cross-validation (GCV) for estimating an appropriate regularization parameter, similar to [29], [35], [51] to obtain the final estimate of the ANS activity. The GCV-FOCUSS+ algorithm requires setting an amplitude threshold parameter manually to get the best results. We instead follow an empirical approach to selecting an amplitude threshold parameter. An initial threshold is selected following [52] and an empirical update rule described in detail in Section II-C2

1) Pre-Processing: Before passing the multichannel SC data to the main algorithm, we process the data to remove unwanted artifacts. A brief overview of the process is given in Fig. 1. First, we filter the signal using a low pass filter with a cut-off frequency of 0.5 Hz to discard the high-frequency noise as the SC signal is known to be band-limited to 0.5 Hz. Then, we downsample the filtered signal to achieve a 1 Hz sampling frequency; hence, the sampling period for the SC signal $T_y = 1\,s$ seconds. To obtain a higher time resolution, a sampling rate $T_u = 0.25$ seconds is used for ANS activity.

2) Problem Formulation: To estimate the unknown parameters u, q, and τ we assume the sparsity constraint on u and including the constraint that the tonic component is always less than or equal to the SC signal, we formulate the following optimization problem,

$$\underset{\substack{u, \tau_r, \tau_d, \\ \alpha, z_{\boldsymbol{\theta}_0}, \boldsymbol{q}}}{\text{minimize}} \; J(\boldsymbol{u}, \boldsymbol{\theta}, \boldsymbol{q}) = \frac{1}{2} \sum_{m=1}^{M} \| y - \mathcal{F}_{\boldsymbol{\theta}_m} z_{\boldsymbol{\theta}_0} - \mathcal{D}_{\boldsymbol{\theta}_m} u$$

$$- G_m \boldsymbol{q}_m \|_2^2 \quad (23)$$

subject to,

$$\tau_{r_{\min}} \le \tau_r \le \tau_{r_{\max}}, \tau_{d_{\min}} \le \tau_d \le \tau_{d_{\max}},$$

$$0 < \alpha, 0 < z_{\boldsymbol{\theta}_0}.$$

We include the l2-norm penalization term with regularization parameter λ_1 to avoid over-fitting while solving for the tonic component coefficients q. The formulation is a sparse recovery problem as $\|u\|_0 \ll M < N$. We encourage the sparsity of u with l_p-norm $(0 < p < 2)$ regularization as a relaxation to the l_0-norm. In particular, we let $p = 0.5$. We can rewrite the optimization problem as follows:

$$\underset{\substack{u, \tau_r, \tau_d, \\ \alpha, z_{\boldsymbol{\theta}_0}, \boldsymbol{q}}}{\text{minimize}} \; J(\boldsymbol{u}, \boldsymbol{\theta}, \boldsymbol{q}) = \frac{1}{2} \sum_{m=1}^{M} (\| y - \mathcal{F}_{\boldsymbol{\theta}_m} z_{\boldsymbol{\theta}_0}$$

$$- \mathcal{D}_{\boldsymbol{\theta}_m} u - G_m \boldsymbol{q}_m \|_2^2$$

$$+ \lambda_1 \|\boldsymbol{q_m}\|_2^2 + \lambda_2 \|\boldsymbol{u}\|_p^p) \quad (24)$$

subject to,

$$\tau_{r_{\min}} \le \tau_r \le \tau_{r_{\max}}, \tau_{d_{\min}} \le \tau_d \le \tau_{d_{\max}},$$

$$0 < \alpha, 0 < z_{\boldsymbol{\theta}_0}.$$

Finally, inspired by the work in [24], [35], we also consider the priors on Skin Conductance Response (SCR) shape parameters.

Algorithm: Concurrent Multichannel Deconvolution.

(a) Let $j = 0$. Initialize $\tilde{\boldsymbol{\theta}}^0$ by uniform sampling from range $[0.10, 1.5]$ for $\tilde{\tau}_{r_m}^{(0)}$, $[1.5, 6]$ for $\tilde{\tau}_{d_m}^{(0)}$, on $[0, y_1]$ for $y_{p_{0_m}}$ $\forall m \in \{1, 2, 3, \ldots, M\}$ and on $[0.01, 1]$ for $\tilde{\alpha}_m^0$, $\forall m \in \{2, 3, \ldots, M\}$; also initialize $\tilde{\boldsymbol{q_m}}^0$ by sampling P Gaussian random variables $\mathcal{N}(0.1, 0.02) \forall m \in \{1, 2, 3, \ldots, M\}$ let and $\tilde{\boldsymbol{Q}}^{(j)} = \{\tilde{q_1}^{(j)}, \tilde{q_2}^{(j)}, \tilde{q_3}^{(j)}, \ldots, \tilde{q_M}^{(j)}\}$.

(b) Set $j = j + 1$.

(c) Set $\boldsymbol{\theta} = \tilde{\boldsymbol{\theta}}^{(j-1)}$ and $\mathbf{Q} = \tilde{\mathbf{Q}}^{(j-1)}$; use FOCUSS+ to solve (25) for $\tilde{\mathbf{u}}^{(j)}$ by initializing $\tilde{\mathbf{u}}^{(j-1)}$ as a vector of all ones.

(d) Set $\mathbf{u} = \tilde{\mathbf{u}}^{(j)}$ and $\mathbf{q} = \tilde{\mathbf{Q}}^{(j-1)}$; use interior point method to minimize (25) and solve for $\tilde{\boldsymbol{\theta}}^{(j)}$ by initializing the at $\tilde{\boldsymbol{\theta}}^{(j-1)}$.

(e) Set $\boldsymbol{\theta} = \tilde{\boldsymbol{\theta}}^{(j)}$ and $\mathbf{u} = \tilde{\mathbf{u}}^{(j)}$; use interior point method to minimize (25) and solve for $\tilde{\mathbf{q}}^{(j)}$ by initializing at $\tilde{\mathbf{Q}}^{(j-1)}$.

(f) Repeat between steps (b)–(e) until $j = 30$.

(g) Let $i = 0$. Set $\hat{\boldsymbol{\theta}}^0 = \tilde{\boldsymbol{\theta}}^{(j)}$, $\hat{\mathbf{u}}^0 = \tilde{\mathbf{u}}^{(j)}$, and $\hat{\mathbf{q}}^0 = \tilde{\mathbf{Q}}^{(j)}$.

(h) Set $i = i + 1$.

(i) Set $\boldsymbol{\theta} = \hat{\boldsymbol{\theta}}^{(i-1)}$ and $\mathbf{Q} = \hat{\mathbf{Q}}^{(i-1)}$; use GCV-FOCUSS+ to solve (25) for $\hat{\mathbf{u}}^{(i)}$ by initializing at $\hat{\mathbf{u}}^{(i-1)}$.

(j) Set $\mathbf{u} = \hat{\mathbf{u}}^{(i)}$ and $\mathbf{Q} = \hat{\mathbf{Q}}^{(i-1)}$; use interior point method to minimize (25) and solve for $\hat{\boldsymbol{\theta}}^{(i)}$ by initializing at $\hat{\boldsymbol{\theta}}^{(i-1)}$.

(k) Set $\boldsymbol{\theta} = \hat{\boldsymbol{\theta}}^{(i-1)}$ and $\mathbf{u} = \hat{\mathbf{u}}^{(i-1)}$; solve (26) to obtain λ_1, and use interior point method to minimize (25) and solve for $\hat{\mathbf{Q}}^{(i)}$ by initializing at $\hat{\mathbf{Q}}^{(i-1)}$.

(l) Iterate between (h)–(k) until convergence.

Fig. 3. Adaptive Threshold Update Rule For FOCUSS+. The update rule for the adaptive FOCUSS algorithm before eliminating impulses below the threshold in each step is shown in (a). The blue impulse is an impulse that is not eliminated in the update step as they are above the threshold and the yellow impulse will be eliminated in the following step. In contrast to the regular GCV-FOCUSS+ algorithm, we amplify the blue impulse instead of leaving it as is. If we draw the wave (marked by a red dotted line) generated by convolving the system model with the blue impulse, the part of the yellow nullified impulses that intersect the wave (marked red) is added to the blue impulse as shown in (b).

We assume that among different individuals, the rise time τ_r and decay times τ_d are Gaussian distributed with means μ_{τ_r} and μ_{τ_d} with corresponding standard deviations σ_{τ_r} and σ_{τ_r}, respectively. The optimization formulation with the priors on the SCR shape parameters becomes as follows:

$$
\begin{aligned}
\underset{\substack{u, \tau_r, \tau_d, \\ \alpha, z_{\boldsymbol{\theta_0}}, \boldsymbol{q}}}{\text{minimize}} \; J(\boldsymbol{u}, \boldsymbol{\theta}, \boldsymbol{q}) = \frac{1}{2} \sum_{m=1}^{M} \Big(& \|y - \mathcal{F}_{\boldsymbol{\theta_m}} z_{\boldsymbol{\theta_0}} \\
& - \mathcal{D}_{\boldsymbol{\theta_m}} \boldsymbol{u} - G_m \boldsymbol{q}_m\|_2^2 \\
& + \lambda_1 \|\boldsymbol{q_m}\|_2^2 + \lambda_2 \|\boldsymbol{u}\|_p^p) \\
& + \frac{\lambda_3}{\sigma_{\tau_r}} \|\tau_r - \mu_{\tau_r}\|_2^2 + \frac{\lambda_4}{\sigma_{\tau_d}} \|\tau_d - \mu_{\tau_d}\|_2^2
\end{aligned}
\tag{25}
$$

subject to,

$$
\tau_{r_{\min}} \leq \tau_r \leq \tau_{r_{\max}}, \tau_{d_{\min}} \leq \tau_d \leq \tau_{d_{\max}},
$$
$$
0 < \alpha, 0 < z_{\boldsymbol{\theta_0}}.
$$

We can solve the inverse problem of finding a sparse nonnegative $\boldsymbol{u}$ by using the FOCUSS+ algorithm [53], which utilizes an iterative least squares (IRLS) approach. We find an initial solution with the FOCUSS+ algorithm. Then we use a modified version of FOCUSS+ called GCV-FOCUSS+ [51] to do the final estimation.

The GCV-FOCUSS+ algorithm is similar to the original FOCUSS algorithm. However, in contrast to FOCUSS and FOCUSS+, GCV-FOCUSS+ solves for $\boldsymbol{u}$ without a fixed number for sparsity, i.e., the upper bound on the number of the non-zero elements. It utilizes the GCV technique to determine the sparse vector $\boldsymbol{u}$. The GCV technique is used for choosing the regularization parameter λ_2 to balance between capturing the noise and the sparsity level of $\boldsymbol{u}$. Zdunek et al. [51] utilized the GCV technique for estimating the value of λ for the FOCUSS+ [54] algorithm with the singular value decomposition as follows:

$$
\min_{\lambda_2} G_2(\lambda_2) = \frac{M \sum_{i=1}^{M} \gamma_i^2 \left(\frac{\lambda_2}{\sigma_i^2 + \lambda_2}\right)^2}{\sum_{i=1}^{M} \left(\frac{\lambda_2}{\sigma_i^2 + \lambda_2}\right)^2}.
$$

subject to $\quad 0 \leq \lambda_2 \leq 1 \times 10^{-4}$ \hfill (26)
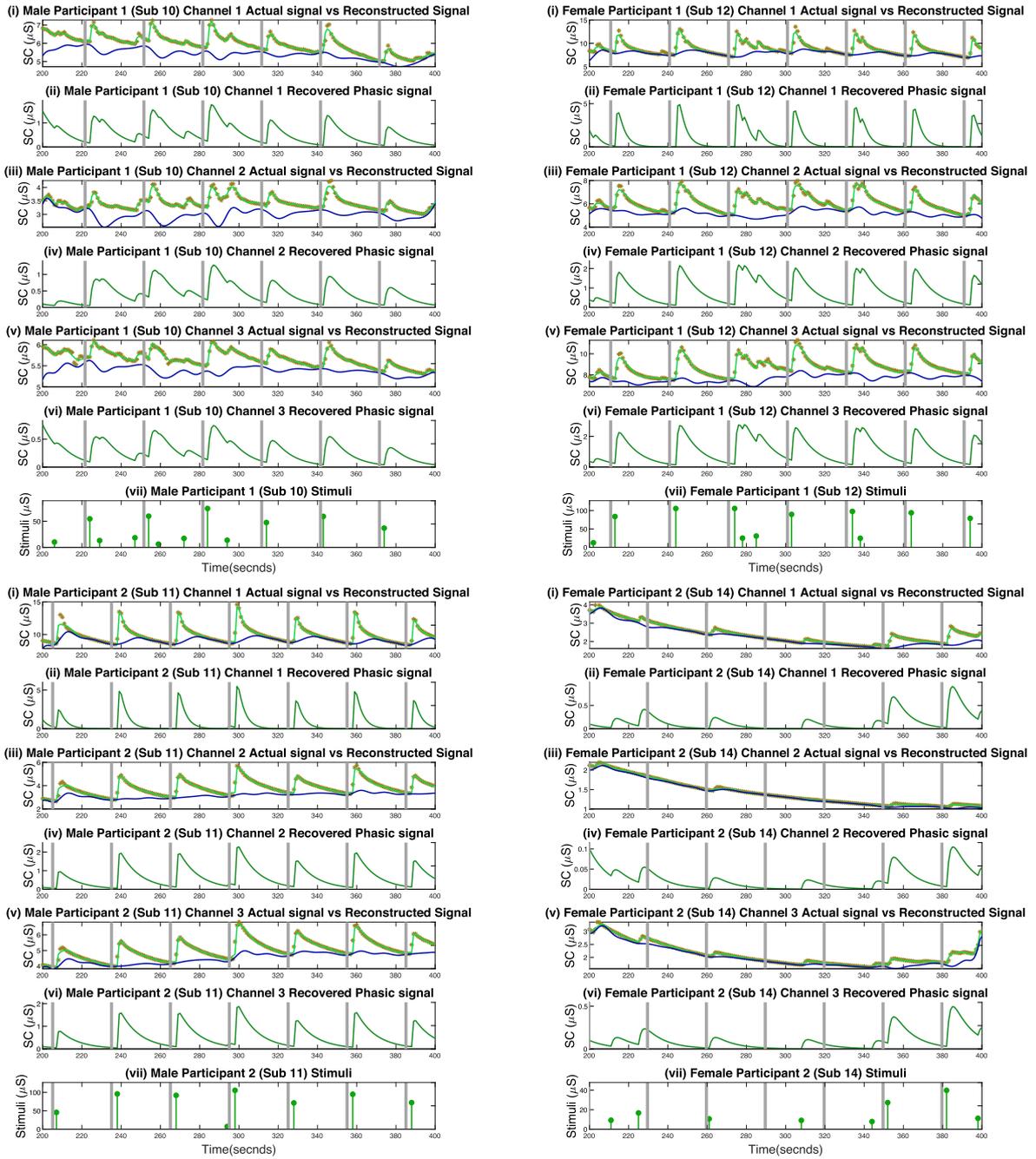
Fig. 4. Estimated Deconvolution of the Experimental Multichannel SC Signals of Two Female and Two Male Participants: In each of the panels, the top sub-panel (i) shows the actual SC signal (orange ∗ markers) versus the reconstructed SC signal (represented by the solid green line) and the tonic component of the signal (solid blue line) for the 1st channel. The timings of the actual stimulation events are shown as gray vertical lines in all panels. (ii) shows the recovered phasic component for channel 1. (iii), (iv), (v), and (vi) show the same figures for channel 2 and channel 3 respectively, and finally (vii) shows the estimated ANS activations.

where $\quad \boldsymbol{\gamma} = \mathbf{R}^\top (y - \mathcal{F}_{\boldsymbol{\theta}_m} z_{\boldsymbol{\theta}_0} - G_m \boldsymbol{q}_m) = [\gamma_1 \ \gamma_2 \ \cdots \ \gamma_M]^\top$ with $\mathcal{D}_{\boldsymbol{\theta}_m} \mathbf{P}_{\mathbf{u}}^{\frac{1}{2}} = \mathbf{R}\boldsymbol{\Sigma}\mathbf{Q}^\top$ with $\mathbf{P}_{\mathbf{u}} = \mathrm{diag}(|\mathbf{u}_i|^{2-p})$ and $\boldsymbol{\Sigma} = \mathrm{diag}\{\sigma_i\}$; $\mathbf{R}$ and $\mathbf{Q}$ are unitary matrices and the σ_i's are the singular values of $\mathbf{B}_\tau \mathbf{P}_{\mathbf{u}}^{\frac{1}{2}}$; N is the total number of data points in $\mathbf{y}$ for each channel. Also here, instead of fixing a manual threshold value, we employ a mini-max thresholding function [52] in the GCV-FOCUSS+ solver. After determining the threshold value K_{th}, we determine all the non-zero elements

in $\hat{u}$ below K. If,

$$\mathcal{I} = \begin{cases} 1 & \hat{u}_n \leq K_{th} \\ 0 & \text{otherwise} \end{cases}$$

$$\mathcal{T}_n = \begin{cases} 1 & n = t \\ 0 & \text{otherwise} \end{cases} \tag{27}$$

Considering $\mathcal{D}_{\boldsymbol{\theta}_1}$ is the matrix formed from the first n rows from matrix $\mathcal{D}_{\boldsymbol{\theta}}$, then we update $\hat{u}_t \ \forall t \mid \hat{u}_t \geq K_{th}$ with the
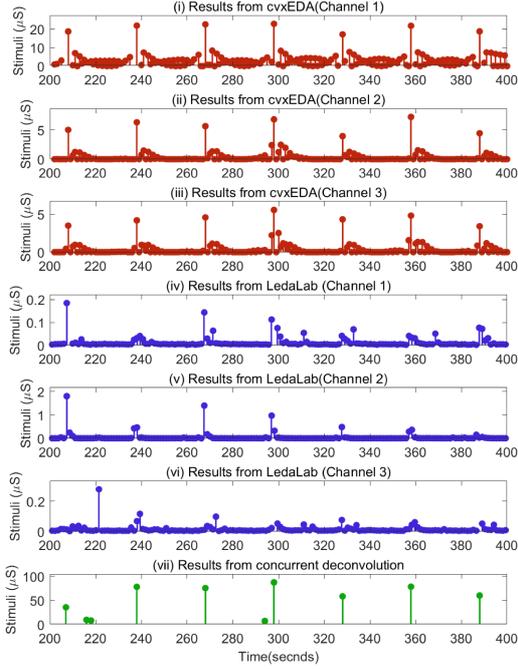
Fig. 5. Comparison of Single Channel Methods with Ours. Panels (i)–(iii) show the deconvolution results of cvxEDA for channels 1–3 respectively, panels (iv)–(vi) show the deconvolution results of Ledalab for channels 1–3 respectively and panel (vii) shows the deconvolution results of our proposed algorithm.

following update rule

$$\hat{u}' = \mathcal{D}_{\boldsymbol{\theta}_1}\left(\hat{u} \odot \mathcal{T}_t\right)$$

$$\hat{u}_t = \hat{u}_t + \sum_n^N \min\left(\hat{u}'_n \odot \mathcal{I}_n, \hat{u}_n \odot \mathcal{I}_n\right) \qquad (28)$$

The equation is illustrated in Fig. 3. In each step of the update, the GCV-FOCUSS+ algorithm nullifies impulses in the predicted impulse train below a set threshold. However, this can often lead to over-sparsity. To constrain this, we use the empirical rule shown in (28) to update the impulse train. Here we convolve each impulse in the impulse train above the threshold separately with the coefficients for the first channel ($\mathcal{D}_{\boldsymbol{\theta}_1}$) from (21) and add the parts of the nullified impulses that fall under the wave. The first channel is used as it is considered the least noisy. In Fig. 3(a), the wave marked in red intersects the nullified impulses at x_1, x_2, and x_3. These portions are then added to the corresponding impulse as done in Fig. 3(b). The motivation for this is that when adjacent impulses are generated due to interference from noise or the tonic component of EDA data, a higher value for the primary impulses will be able to drown out the secondary ones generated due to the interference and thereafter allow the tonic component to fit to the residual. In the case of regular GCV-FOCUSS+, the algorithm may overfit the tonic component due to the interference causing over-sparsity.

For $r = 0, 1, 2, \cdots$, Our modified GCV-FOCUSS+ works as follows [29]:

1) $\mathbf{P}_{\mathbf{u}}^{(r)} = \mathrm{diag}(|\mathbf{u}_i^{(r)}|^{2-p})$
2) $\mathbf{u}^{(r+1)} = \mathbf{P}_{\mathbf{u}}\mathbf{B}_{\boldsymbol{\tau}}^{\top}(\mathbf{B}_{\boldsymbol{\tau}}\mathbf{P}_{\mathbf{u}}\mathbf{B}_{\boldsymbol{\tau}}^{\top} + \lambda_2\boldsymbol{I})^{-1}\boldsymbol{y}_{\theta}$
3) Update $\mathbf{u}^{(r+1)}$ as per (28)
4) $\lambda_2^{(r+1)} = \arg\min_{0 \le \lambda_2 \le 1 \times 10^{-4}} G_2(\lambda_2)$
5) Iterate until convergence

To solve for the physiological system parameter in $\boldsymbol{\theta}$, we solve the optimization problem in (25) using the interior point method.

III. RESULTS AND DISCUSSION

A. Response to Auditory Stimuli

Comparing ANS activations recovered by deconvolving the SC response using different methods is not a conclusive evaluation as the original stimulus is unknown. Nevertheless, we can do several ablation studies to show that the results of the methods we propose are both grounded in their assumptions and justified in their outputs. One way we can show that the deconvolved signal is correct is to compare the position and magnitude of the ANS activations with respect to auditory stimuli during the experiment. Using the proposed approach, we decompose the SC measurements collected during the auditory stimulation experiment described in [49] using our approach and separate the tonic and phasic components. Furthermore, we recover the underlying stimuli $u(t)$, the corresponding rise time (τ_r), decay times (τ_d), and the initial phasic SC conditions for each channel y_{p_0}. We show the results in Fig. 4 to demonstrate that the proposed algorithm successfully estimates the tonic and phasic components along with the timing and amplitudes of ANS activations for two male participants and two female participants. For additional results, please see Figs. 9–13. Note that some subjects like the Female participant 12 in Fig. 12 and the male Participant 11 in Figs. 13 have a lot of noise and some portions of the data are illegible. We keep those results however for reference.

B. Comparison to Other Approaches

Although a direct comparison cannot be shown, we demonstrate our algorithm's ability to generate a more sparse signal with multi-channel data compared to single-channel approaches like cvxEDA and Ledalab while maintaining a higher goodness of fit. Our proposed algorithm can recover the ANS activations while suppressing noise. This is in stark contrast to cvxEDA and ledalab whose results are much less sparse. A comparison is shown in Fig. 5.

This shows that the proposed algorithm is much more resilient to input noise and can suppress impulses from noise. This is essential as SC signals tend to get contaminated with noise in real-world scenarios [12], [37].

C. Influence of Number of Channels

The primary focus of this work is to use multiple channels to build a more resilient algorithm for SC deconvolution. To justify that our approach indeed improves upon the existing single-channel approach described in [34], [55], [56], [57], we show the
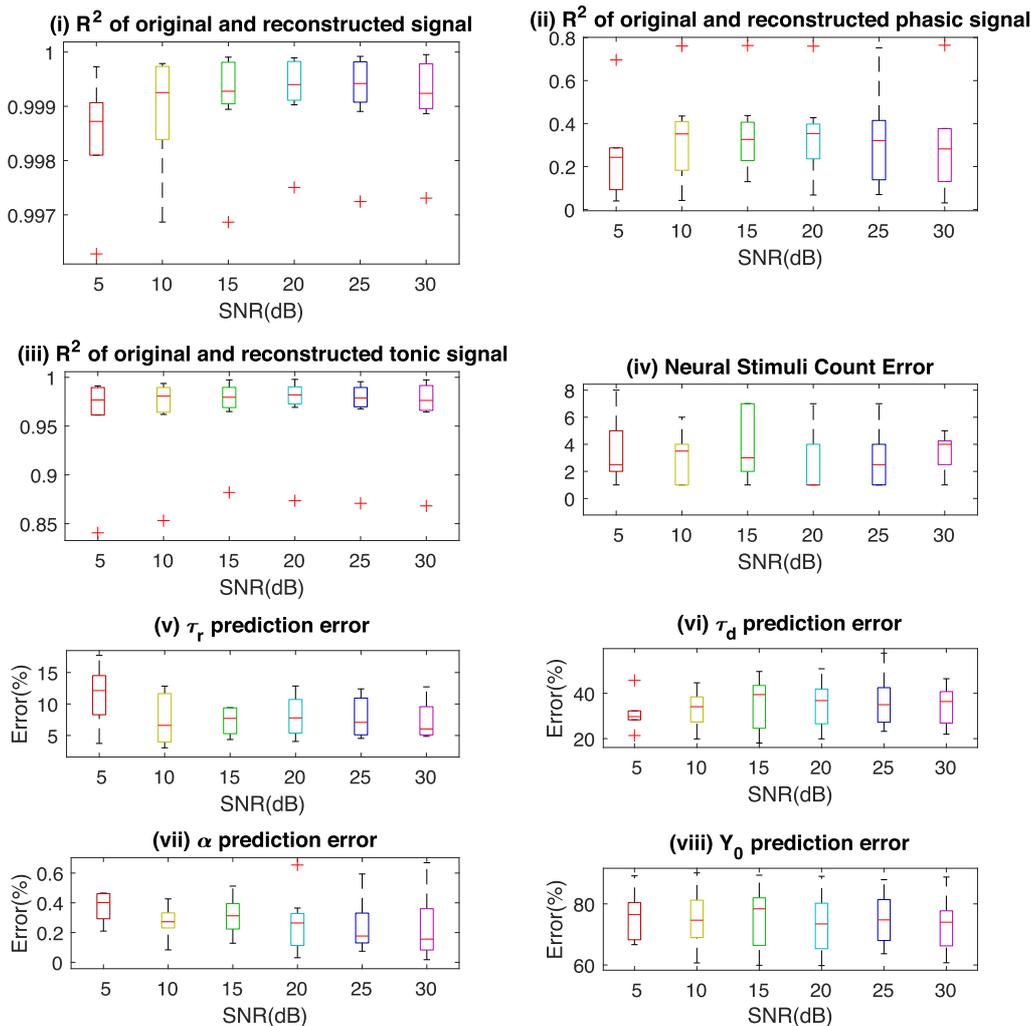
Fig. 6.   Reconstruction Performance of Our Algorithm with Simulated Noise The solid line in the above panels shows the mean value and the vertical limits are variances of the metric for a particular noise level overall simulated subjects. Panel (i)–(iii) shows the change in R^2 value between the recovered signal and original signal for SC signal, phasic component, and tonic component respectively. Panel (iv) shows the difference between the non-zero count of the recovered sparse signal to the original. Panel (v)–(viii) shows the percentage error of recovered parameters τ_r, τ_d, α, and Y_0 respectively.

TABLE I
COMPARISON OF PREDICTION ERRORS WITH DIFFERENT CHANNEL CONFIGURATIONS

Channel Configuration	$\frac{||\tau_r - \hat{\tau}_r||_1}{\tau_r}(\%)$	$\frac{||\tau_d - \hat{\tau}_d||_1}{\tau_d}(\%)$	$\frac{||Y_0 - \hat{Y}_0||_1}{||Y_0||_1}(\%)$	$\frac{||Y - \hat{Y}||_2}{||Y||_2}(\%)$	$\frac{||Y_p - \hat{Y}_p||_2}{||Y_p||_2}(\%)$	$\frac{||Y_s - \hat{Y}_s||_2}{||Y_s||_2}(\%)$	$\frac{||u - \hat{u}||_2}{||u||_2}(\%)$	$\| ||u||_0 - ||\hat{u}'||_0 \|$
1	5.3	73.5	59.2	0.4	35.0	3.4	10.9	1.25
2	12.3	92.5	76.2	2.0	71.1	3.4	80.7	6.125
3	14.4	54.2	82.6	0.9	75.4	4.4	63.6	3.5
1, 2	4.0	47.3	68.8	0.2	18.3	1.6	11.2	1.375
1, 3	6.2	31.7	66.0	0.2	25.8	1.9	16.3	1.25
2, 3	7.8	63.9	80.8	0.7	50.4	3.5	82.8	5.0
1, 2, 3	**2.7**	**30.3**	**69.5**	**0.1**	**17.4**	**1.4**	**12.3**	**1.125**

performance of our algorithm with respect to the configuration of different channels. Here, we use simulated data obtained from the results of using our approach on the dataset in [49] as a reference. We recompute the simulated data and show the errors of different parameters in Table I.

From prior work [58], [59] and from experimental observation, we see that Channel 1, derived from the thenar/hypothenar of the non-dominant hand has the most relevant information and a single channel configuration works best in this channel. However, the inclusion of multiple channels is
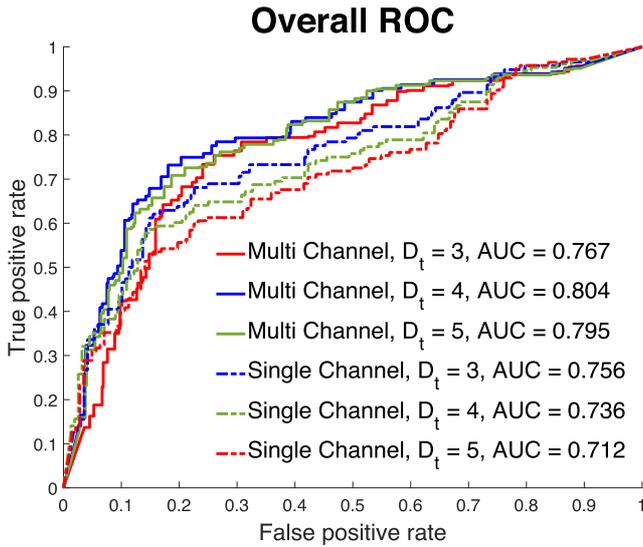
Fig. 7. ROC Curves for Single vs Multichannel Decomposition. ROC curves of single channel deconvolution done previously in [39] (indicated by dashed lines) compared to multichannel deconvolution (indicated by solid lines) are shown above for lookback durations 3 s (red), 4 s (green) and 5 s (blue). The average ROC for all subjects is also marked.

Fig. 8. Analysis of Rise and Decay Times. A segment of skin conductance data for subject 1 is shown. Note how the delay between channel 1 (red) and channel 2 (blue) indicated as β_2 decreases from 1.01 s to 0.51 s whereas the delay between channel 1 and channel 3 (yellow) indicated as β_3 decreases from 1.66 s to 1.34 s. There is also a missing impulse in channel 3 that is present in both channel 1 and channel 2.

able to improve the predicted parameters without over-fitting to noise. A significant advantage of using multiple channels is the improved prediction of the number of impulses as well as the reconstruction error. Since Y_p falls exponentially with a much longer decay time, the influence of Y_p on the main signal Y during the downward slope after some time is heavily diminished. Hence, the models tend to converge to widely different values of τ_d. This is true for Y_0 as well since its value only influences the initial part of the signal after which its influence greatly diminishes.

D. Analyzing Robustness of Model

To demonstrate the robustness of the algorithm, we also show the effect of the prediction errors with respect to increasing corruption of the SC signals with noise. This is shown in Fig. 6. Most estimation errors drop down with noise reduction. However, the recovered timings and number of impulses remain nearly the same on average albeit showing higher variance with higher noise.

We can also check the robustness of the approach by calculating ROC [60], [61], [62]. However, comparing two sparse signals is not straightforward. Thus, we follow the approach in [35] to calculate ROC. We assume the problem to be that of binary classification. Based on any detected impulse we check for impulses with a look back duration, D_t s behind in the actual simulated data. If there is an impulse within that time frame we consider it a true positive otherwise, it is considered a false positive. Compared to [35] which has an average ROC of 0.736 at $D_t = 4$ s, ours has a ROC of 0.804 for the same time range. We can see a detailed comparison in Fig. 7 where our algorithm outperforms the single channel deconvolution for all look-back durations. The ROC curves of ledaLab and cvxEDA for each channel are shown in Fig. 14. We can also see this in Table I done for simulated data. We define a parameter $\hat{u}'$ which takes

the maximum within a 5 s window of a ground truth impulse and masks all residual impulses in that window. We then compare the zero norm of the signals. We can see that our proposed model performs better in terms of capturing all ground truth impulses here as well. Note that the ROC is 0.747 if we do not modify the GCV-FOCUSS+ algorithm according to (28).

E. Missing Impulses and Variable Delay

In our model, to simplify the problem similar to [35], we assumed that the delay between channels (β_i) is constant and that the underlying phasic signal for each channel can be represented as a scaled and delayed version of a reference channel. We have found that the delay is not constant but rather it can change. The channels can even have missing impulses. An example of this is shown in Fig. 8. Here we see that the delay for the second channel β_2 changes from 1.01 s to 0.51 s. A similar situation is seen for β_3. We also see a missing impulse denoted in the figure. The algorithm optimizes for the delay that reduces the error over the entire signal, which, given enough impulses shows good accuracy. However, if a signal has a small number of underlying impulses, the model will fail to reconstruct the signal accurately. In such cases, the variability of delay could be integrated into the model for more accurate deconvolution results. The modeling of missing skin conductance responses in a couple of channels is a problem that requires further investigation (see Fig. 8). The missing impulses could arise from the non-linearity of the system, for example, different channels could have different thresholds below which responses are not seen on the SC data. Another way to model this could be to consider the ANS activity as originating from multiple sources. In this case, stimuli from different sources may only register on certain channels corresponding to different parts of the body. The cause for the missing skin conductance responses whether it is due to system
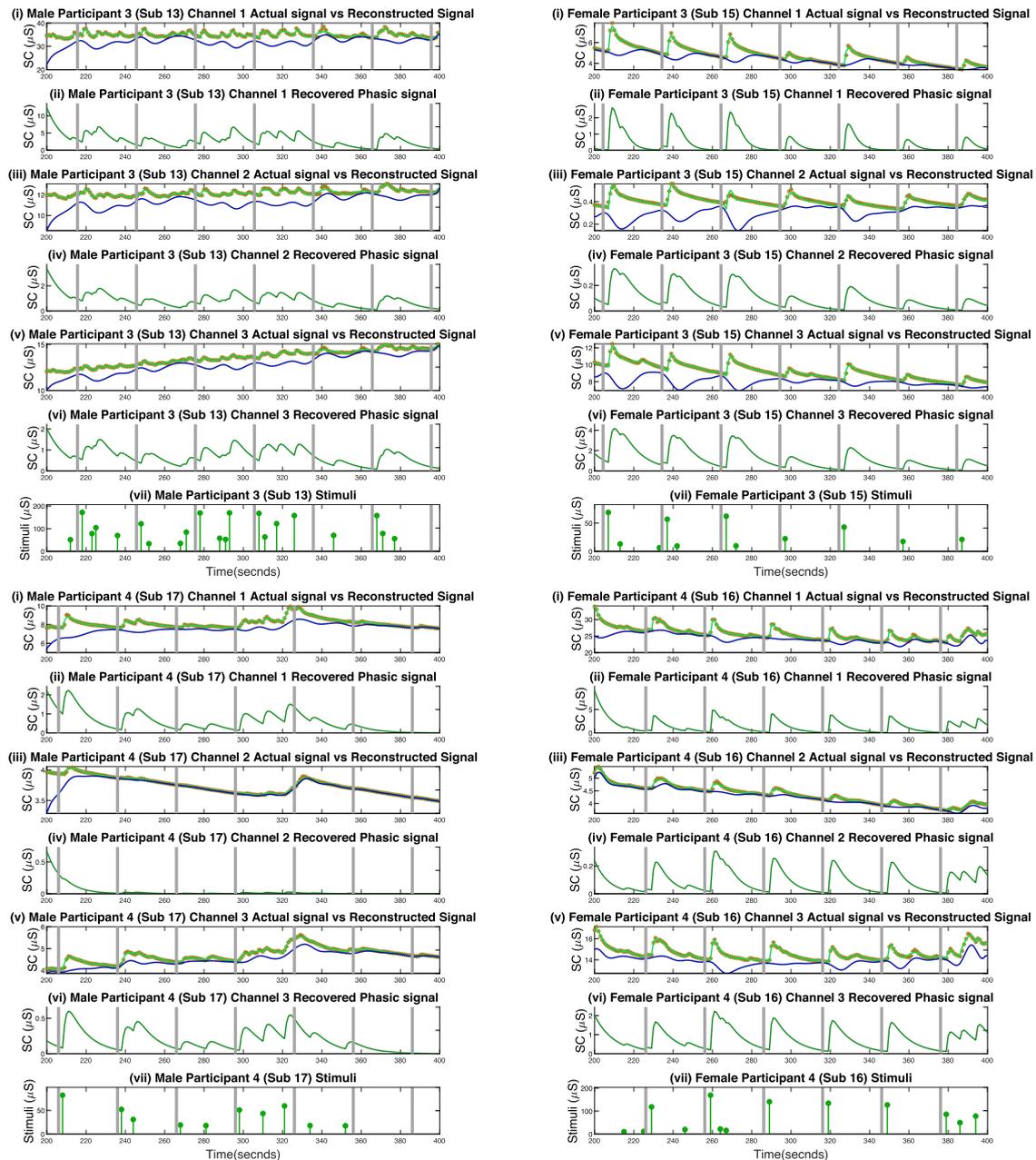
Fig. 9. Estimated Deconvolution of the Experimental Multi-Channel SC Signals of Two Female and Two Male Participants: In each of the panels, the top sub-panel (i) shows the actual SC signal (orange ∗ markers) versus the reconstructed SC signal (represented by the solid green line) and the tonic component of the signal (solid blue line) for the 1st channel. The timings of the actual stimulation events are shown as gray vertical lines in all panels. (ii) shows the recovered phasic component for channel 1. (iii), (iv), (v), and (vi) show the same figures for channel 2 and channel 3, respectively, and finally (vii) shows the estimated ANS activations.

non-linearity or physiological modeling of the system is an interesting research prospect, but it is outside the scope of this work. Hence, it is left for future investigations.

IV. LIMITATIONS AND FUTURE WORK

While the use of multi-channel deconvolution enhances the robustness of results, it introduces computational challenges due to the non-linear scaling of computation time. Specifically, the single-channel algorithm employed in this study relies on matrix inversion, an operation characterized by a computational complexity of $O(n^3)$. Consequently, extending this algorithm to accommodate multiple channels significantly prolongs computation time.

For instance, the average runtime of our algorithm is approximately 4.8 hours, in stark contrast to the 8 seconds and 182 seconds needed for cvxEDA and LedaLab, respectively. Despite the longer processing time, it is crucial to note that neither cvxEDA nor LedaLab are equipped to handle multi-channel data, thereby limiting their applicability.

That being said, recent research [24] has unveiled promising solutions to circumvent these computational complexity issues.
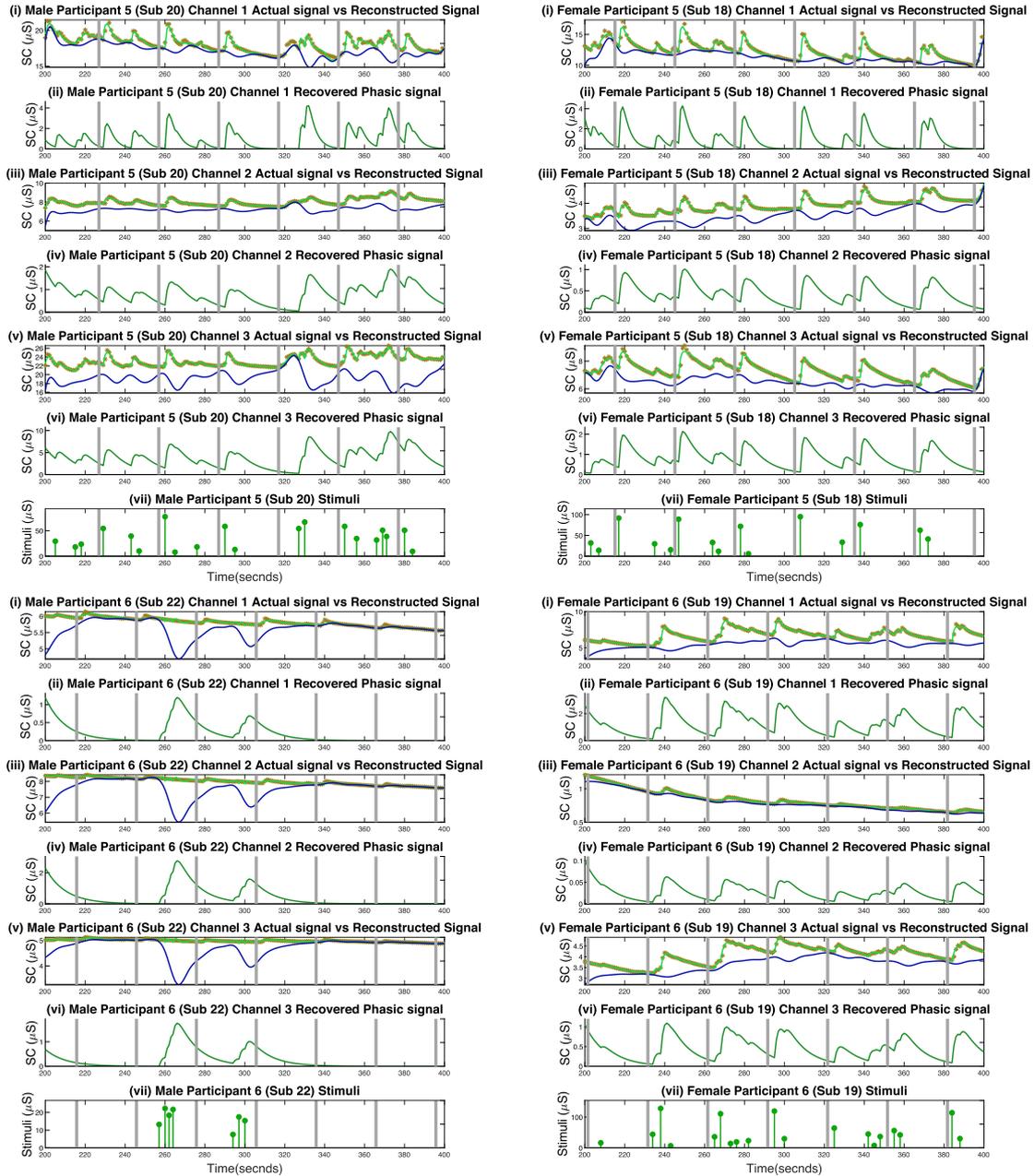
Fig. 10. Estimated Deconvolution of the Experimental Multi-Channel SC Signals of Two Female and Two Male Participants: In each of the panels, the top sub-panel (i) shows the actual SC signal (orange * markers) versus the reconstructed SC signal (represented by the solid green line) and the tonic component of the signal (solid blue line) for the 1st channel. The timings of the actual stimulation events are shown as gray vertical lines in all panels. (ii) shows the recovered phasic component for channel 1. (iii), (iv), (v), and (vi) show the same figures for channel 2 and channel 3, respectively, and finally (vii) shows the estimated ANS activations.

As such, future work can capitalize on these advancements, and focus on developing strategies for efficiently processing multi-channel inputs, thereby expanding the capability of our algorithm while ensuring computational feasibility.

V. CONCLUSION

It is quite challenging to decode SC data to predict the estimated ANS activations along with the rise and decay times of

the SC responses. The proposed algorithm has many degrees of freedom that make it likely to run into overfitting problems. There exist many solutions for the unknowns that can closely approximate the sampled signal. The system is under-determined which makes it more susceptible to noise. However, incorporating sufficient physiological constraints can simplify the search space of the problem. We imposed several constraints. The first is the sparsity constraint on the ANS activations as done in [35], [39]. Additionally, we constrain the values of the rise
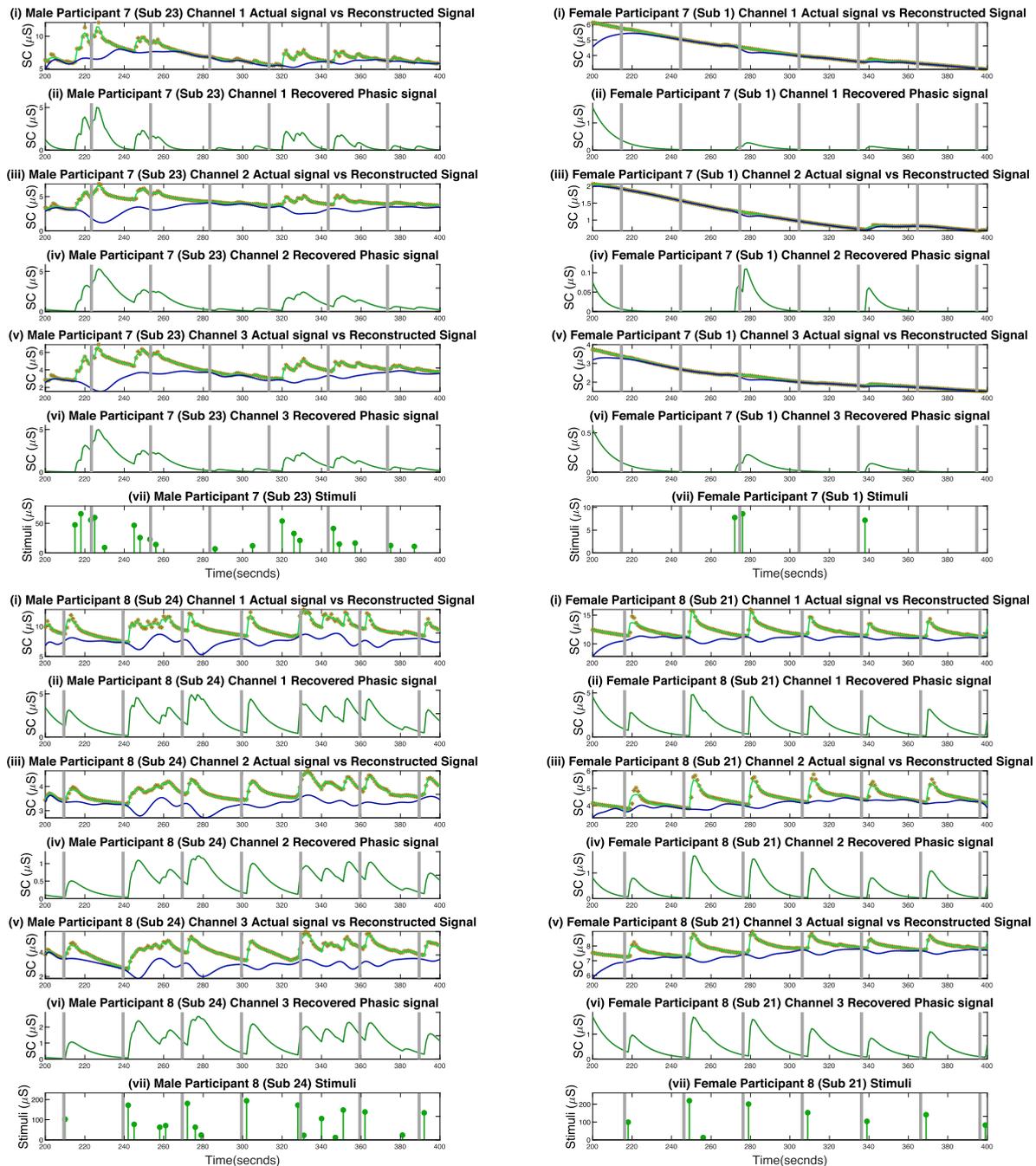
Fig. 11. Estimated Deconvolution of the Experimental Multi-Channel SC Signals of Two Female and Two Male Participants: In each of the panels, the top sub-panel (i) shows the actual SC signal (orange ∗ markers) versus the reconstructed SC signal (represented by the solid green line) and the tonic component of the signal (solid blue line) for the 1st channel. The timings of the actual stimulation events are shown as gray vertical lines in all panels. (ii) shows the recovered phasic component for channel 1. (iii), (iv), (v), and (vi) show the same figures for channel 2 and channel 3, respectively, and finally (vii) shows the estimated ANS activations.

and decay times to fixed ranges between $\tau^{min} = [0.1 \ \ 1.4]$ and $\tau^{max} = [1.5 \ \ 6]$. We further constrain α in the range $[10^{-2} \ 10]$ and y_{p_0} in the range $[0 \ y_1]$ We also impose constraints on the smoothness of the cubic B-spline basis function by including l_2-norm penalization. Finally, we employ the GCV technique and adaptive thresholding to have appropriate estimates of λ to achieve a balance between capturing the data and residual error.

There is also the likelihood that the optimization may stagnate at local minima. Therefore, we initialize the optimization problem with several random initializations for τ_r, τ_d, and y_0. Among all the deconvolution results using this random initialization, we choose the one that minimizes the least square reconstruction error. It is still possible to reach a suboptimal solution, however using multiple initializations, our proposed algorithm works
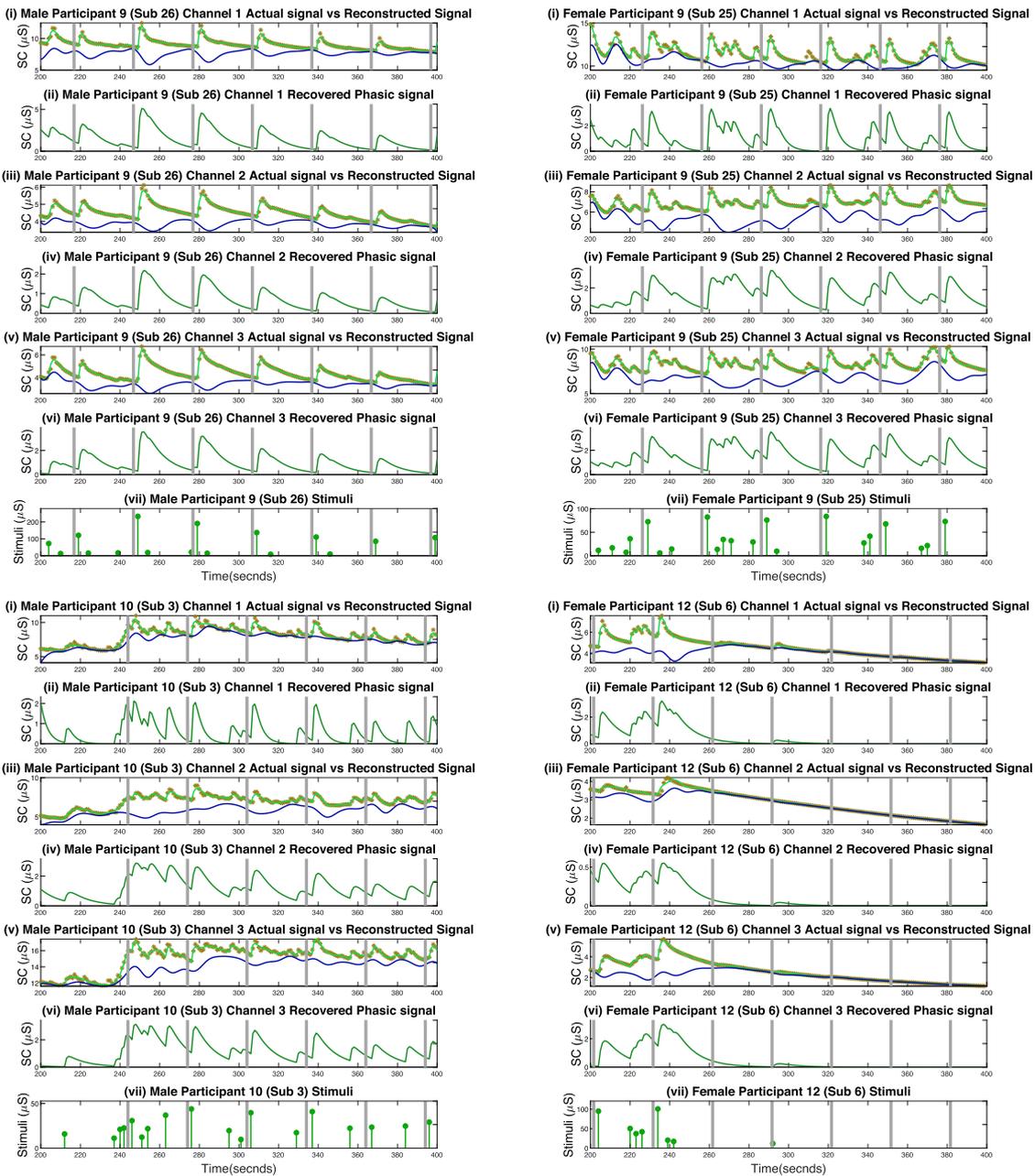
Fig. 12. Estimated Deconvolution of the Experimental Multi-Channel SC Signals of Two Female and Two Male Participants: In each of the panels, the top sub-panel (i) shows the actual SC signal (orange ∗ markers) versus the reconstructed SC signal (represented by the solid green line) and the tonic component of the signal (solid blue line) for the 1st channel. The timings of the actual stimulation events are shown as gray vertical lines in all panels. (ii) shows the recovered phasic component for channel 1. (iii), (iv), (v), and (vi) show the same figures for channel 2 and channel 3, respectively, and finally (vii) shows the estimated ANS activations.

well in modeling SCR shape. The use of multichannel data also increases the likelihood of capturing stray impulses. For SC data in the PsPm-SCRV10 dataset, in particular, the 1st channel is usually the cleanest while the 3rd is the noisiest. This is shown in Table I. We see that single channel results for 2nd and 3rd are much worse than the 1st channel. If we check the SC data for each channel, we can see that some channels do not show all the same impulses. To minimize this, we use correlation-based

delay estimation to align all impulses. However, the delay between impulses is not fixed and we have found that the delay between impulses can vary slowly over time. This cannot be properly estimated with a correlation-based delay estimation and must be included in the system itself to be properly modeled. However, using a combination of these channels, better results can generally be obtained. In our proposed algorithm, we focused on reducing the number of missed impulses by altering
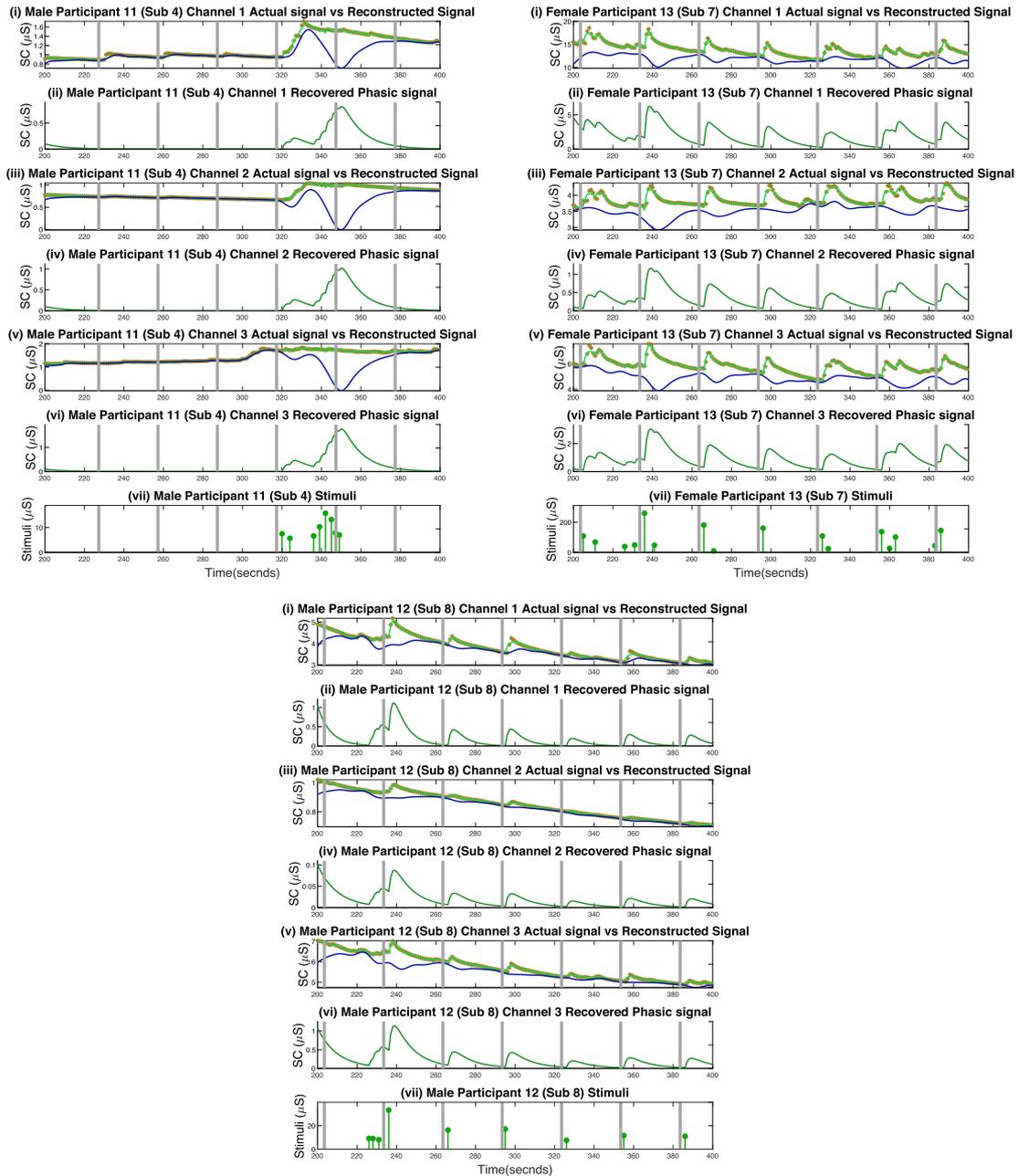
Fig. 13. Estimated Deconvolution of the Experimental Multi-Channel SC Signals of One Female and Two Male Participants: In each of the panels, the top sub-panel (i) shows the actual SC signal (orange ∗ markers) versus the reconstructed SC signal (represented by the solid green line) and the tonic component of the signal (solid blue line) for the 1st channel. The timings of the actual stimulation events are shown as gray vertical lines in all panels. (ii) shows the recovered phasic component for channel 1. (iii), (iv), (v), and (vi) show the same figures for channel 2 and channel 3, respectively, and finally (vii) shows the estimated ANS activations.

the GCV-FOCUSS+ algorithm. For future work, we plan to use the state-space modeling of SC and implement a Bayesian inference framework to reduce the time complexity. Novel ways to incorporate varying time delays and missing impulses in SC channels into the state-space model can also be scope for future research. Once a real-time algorithm is developed that is resilient to noise, it can be integrated into a system for arousal regulation where the output of the algorithm can be used as the control signal for estimating the arousal state.
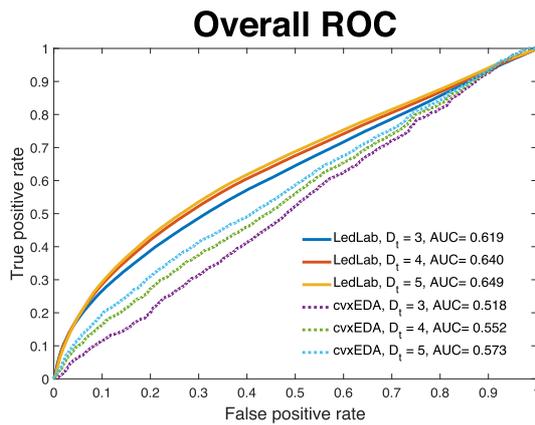
Fig. 14. ROC curves for LedaLab and cvxEDA.

Conflict of Interest: Samiul Alam has no conflicts of interest to declare. Rose T. Faghih and Md. Rafiul Amin are co-inventors in a patent application related to this research filed by the University of Houston.

REFERENCES

[1] H. Critchley and Y. Nagai, *Electrodermal Activity (EDA)*. New York, NY, USA: Springer, 2013.

[2] J. Boulant, "Hypothalamic mechanism in thermoregulation," *Federation Proc.*, vol. 40, pp. 2843–50, 1982.

[3] J. L. Andreassi, *Psychophysiology - Human Behavior and Physiological Response*. London, U.K.: Psychol. Press, 2013.

[4] R. W. Picard and J. Scheirer, "The galvactivator: A glove that senses and communicates skin conductivity," in *Proc. 9th Int. Conf. HCI*, 2001, pp. 1538–1542.

[5] Y. B. Lee, S. W. Yoon, C. K. Lee, and M. H. Lee, "Wearable EDA sensor gloves using conducting fabric and embedded system," in *World Congress on Medical Physics and Biomedical Engineering 2006*, R. Magjarevic and J. H. Nagel, Eds. Berlin, Heidelberg: Springer, 2007, pp. 883–888.

[6] L. Fraiwan, T. Basmaji, and O. Hassanin, "A mobile mental health monitoring system: A smart glove," in *Proc. 14th Int. Conf. Signal-Image Technol. Internet-Based Syst.*, 2018, pp. 235–240.

[7] D. Alexander, C. Trengove, P. Johnston, T. Cooper, J. August, and E. Gordon, "Separating individual skin conductance responses in a short interstimulus-interval paradigm," *J. Neurosci. Methods*, vol. 146, no. 1, pp. 116–123, 2005. [Online]. Available: https://www.sciencedirect.com/science/article/pii/S0165027005000464

[8] W. Boucsein, *Electrodermal Activity* (The Springer Series in Behavioral Psychophysiology and Medicine Series). New York, NY, USA: Springer, 2012. [Online]. Available: https://books.google.com.bd/books?id=6N6rnOEZEEoC

[9] M. Benedek and C. Kaernbach, "A continuous measure of phasic electrodermal activity," *J. Neurosci. Methods*, vol. 190, no. 1, pp. 80–91, 2010.

[10] M. Benedek and C. Kaernbach, "Decomposition of skin conductance data by means of nonnegative deconvolution," *Psychophysiol.*, vol. 47, no. 4, pp. 647–658, 2010.

[11] A. Greco, G. Valenza, A. Lanata, E. P. Scilingo, and L. Citi, "cvxEDA: A convex optimization approach to electrodermal activity processing," *IEEE Trans. Biomed. Eng.*, vol. 63, no. 4, pp. 797–804, Apr. 2016.

[12] J. J. Braithwaite, D. G. Watson, R. Jones, and M. Rowe, "A guide for analysing electrodermal activity (EDA) & skin conductance responses (SCRS) for psychological experiments," *Psychophysiology*, vol. 49, no. 1, pp. 1017–1034, 2013.

[13] D. S. Wickramasuriya and R. T. Faghih, "A Bayesian filtering approach for tracking arousal from binary and continuous skin conductance features," *IEEE Trans. Biomed. Eng.*, vol. 67, no. 6, pp. 1749–1760, Jun. 2020.

[14] W. B. Mendes, *Assessing Autonomic Nervous System Activity* (Methods in Social Neuroscience Series). New York, NY, USA: Guilford Press, 2009, pp. 118–147.

[15] A. Y. Kim et al., "Skin conductance responses in major depressive disorder (MDD) under mental arithmetic stress," *Plos One*, vol. 14, no. 4, pp. 1–13, 2019, doi: 10.1371/journal.pone.0213140.

[16] E. W. Geldreich, "Skin conductance changes occurring during mental fatigue," *Trans. Kansas Acad. Sci. (1903-)*, vol. 42, pp. 393–395, 1939. [Online]. Available: http://www.jstor.org/stable/3625100

[17] G. L. Poerio, E. Blakey, T. J. Hostler, and T. Veltri, "More than a feeling: Autonomic sensory meridian response (ASMR) is characterized by reliable changes in affect and physiology," *PLoS One*, vol. 13, no. 6, pp. 1–18, 2018, doi: 10.1371/journal.pone.0196645.

[18] J. Wijsman, B. Grundlehner, H. Liu, H. Hermens, and J. Penders, "Towards mental stress detection using wearable physiological sensors," in *Proc. IEEE Annu. Int. Conf. Eng. Med. Biol. Soc.*, 2011, pp. 1798–1801.

[19] Y. Khan et al., "Design considerations of a wearable electronic-skin for mental health and wellness: Balancing biosignals and human factors," *bioRxiv*, 2021. [Online]. Available: https://www.biorxiv.org/content/early/2021/01/21/2021.01.20.427496

[20] N. Long, Y. Lei, L. Peng, P. Xu, and P. Mao, "A scoping review on monitoring mental health using smart wearable devices," *Math. Biosci. Eng.*, vol. 19, no. 8, pp. 7899–7919, 2022.

[21] B. A. Hickey et al., "Smart devices and wearable technologies to detect and monitor mental health conditions and stress: A systematic review," *Sensors*, vol. 21, no. 10, 2021, Art. no. 3461.

[22] L. S. Too, M. Spittal, L. Bugeja, L. Reifels, P. Butterworth, and J. Pirkis, "The association between mental disorders and suicide: A systematic review and meta-analysis of record linkage studies," *J. Affect. Disord.*, vol. 259, pp. 302–313, 2019.

[23] Y. S. Can, N. Chalabianloo, D. Ekiz, and C. Ersoy, "Continuous stress detection using wearable sensors in real life: Algorithmic programming contest case study," *Sensors*, vol. 19, no. 8, 2019, Art. no. 1849.

[24] R. Amin and R. T. Faghih, "Physiological characterization of electrodermal activity enables scalable near real-time autonomic nervous system activation inference," *PLoS Comput. Biol.*, vol. 18, no. 7, pp. 1–28, 2022, doi: 10.1371/journal.pcbi.1010275.

[25] M. R. Amin, D. D. Pednekar, H. F. Azgomi, H. van Wietmarschen, K. Aschbacher, and R. T. Faghih, "Sparse system identification of leptin dynamics in women with obesity," *Front. Endocrinol.*, vol. 13, 2022, Art. no. 769951. [Online]. Available: https://www.frontiersin.org/articles/10.3389/fendo.2022.769951

[26] R. T. Faghih et al., "Characterization of fear conditioning and fear extinction by analysis of electrodermal activity," in *Proc. IEEE 37th Annu. Int. Conf. Eng. Med. Biol. Soc.*, Aug. 2015, doi: 10.1109/embc.2015.7320204.

[27] M. R. Amin and R. T. Faghih, "Sparse deconvolution of electrodermal activity via continuous-time system identification," *IEEE Trans. Biomed. Eng.*, vol. 66, no. 9, pp. 2585–2595, Sep. 2019.

[28] R. T. Faghih, "System identification of cortisol secretion: Characterizing pulsatile dynamics," Ph.D. dissertation, Massachusetts Inst. Technol.,Cambridge, MA, USA, 2014.

[29] R. T. Faghih, M. A. Dahleh, G. K. Adler, E. B. Klerman, and E. N. Brown, "Deconvolution of serum cortisol levels by using compressed sensing," *PLoS One*, vol. 9, no. 1, 2014, Art. no. e85204.

[30] R. T. Faghih, M. A. Dahleh, G. K. Adler, E. B. Klerman, and E. N. Brown, "Quantifying pituitary-adrenal dynamics and deconvolution of concurrent cortisol and adrenocorticotropic hormone data by compressed sensing," *IEEE Trans. Biomed. Eng.*, vol. 62, no. 10, pp. 2379–2388, Oct. 2015.

[31] R. T. Faghih, "From physiological signals to pulsatile dynamics: A sparse system identification approach," in *Dynamic Neuroscience*. Berlin, Germany: Springer, 2018, pp. 239–265.

[32] D. D. Pednekar, M. R. Amin, H. F. Azgomi, K. Aschbacher, L. J. Crofford, and R. T. Faghih, "Characterization of cortisol dysregulation in fibromyalgia and chronic fatigue syndromes: A state-space approach," *IEEE Trans. Biomed. Eng.*, vol. 67, no. 11, pp. 3163–3172, Nov. 2020.

[33] D. D. Pednekar, M. R. Amin, H. F. Azgomi, K. Aschbacher, L. J. Crofford, and R. T. Faghih, "A system theoretic investigation of cortisol dysregulation in fibromyalgia patients with chronic fatigue," in *Proc. IEEE 41st Annu. Int. Conf. Eng. Med. Biol. Soc.*, 2019, pp. 6896–6901.

[34] M. R. Amin and R. T. Faghih, "Tonic and phasic decomposition of skin conductance data: A generalized-cross-validation-based block coordinate descent approach," in *Proc. IEEE 41st Annu. Int. Conf. Eng. Med. Biol. Soc.*, 2019, pp. 745–749.

[35] M. R. Amin and R. T. Faghih, "Robust inference of autonomic nervous system activation using skin conductance measurements: A multi-channel sparse system identification approach," *IEEE Access*, vol. 7, pp. 173419–173437, 2019.

[36] M. R. Amin and R. T. Faghih, "Inferring autonomic nervous system stimulation from hand and foot skin conductance measurements," in *Proc. IEEE 52th Asilomar Conf. Signals, Syst. Comput.*, 2018, pp. 655–660.

[37] D. R. Bach, K. J. Friston, and R. J. Dolan, "An improved algorithm for model-based analysis of evoked skin conductance responses," *Biol. Psychol.*, vol. 94, no. 3, pp. 490–497, 2013.

[38] Z. Ghasemi et al., "Estimation of cardiovascular risk predictors from non-invasively measured diametric pulse volume waveforms via multiple measurement information fusion," *Sci. Rep.*, vol. 8, no. 1, pp. 1–11, 2018.

[39] M. R. Amin and R. T. Faghih, "Identification of sympathetic nervous system activation from skin conductance: A sparse decomposition approach with physiological priors," *IEEE Trans. Biomed. Eng.*, vol. 68, no. 5, pp. 1726–1736, May 2021.

[40] O. T. Inan et al., "Ballistocardiography and seismocardiography: A review of recent advances," *IEEE J. Biomed. Health Inform.*, vol. 19, no. 4, pp. 1414–1427, Jul. 2015.

[41] B. C. Callaghan, H. T. Cheng, C. L. Stables, A. L. Smith, and E. L. Feldman, "Diabetic neuropathy: Clinical manifestations and current treatments," *Lancet Neurol.*, vol. 11, no. 6, pp. 521–534, Jun. 2012, doi: 10.1016/s1474-4422(12)70065-0.

[42] C. M. Casellini, H. K. Parson, M. S. Richardson, M. L. Nevoret, and A. I. Vinik, "Sudoscan, a noninvasive tool for detecting diabetic small fiber neuropathy and autonomic dysfunction," *Diabetes Technol. Therapeutics*, vol. 15, no. 11, pp. 948–953, 2013, doi: 10.1089/dia.2013.0129.

[43] A. Cichocki et al., "Tensor decompositions for signal processing applications: From two-way to multiway component analysis," *IEEE Signal Process. Mag.*, vol. 32, no. 2, pp. 145–163, Mar. 2015.

[44] I. Daubechies, *Ten Lectures on Wavelets*. Philadelphia, PA, USA: SIAM, 1992.

[45] D. C. Fowles, M. J. Christie, R. Edelberg, W. W. Grings, D. T. Lykken, and P. H. Venables, "Publication recommendations for electrodermal measurements," *Psychophysiology*, vol. 18, no. 3, pp. 232–239, 1981.

[46] M. E. Dawson, A. M. Schell, and D. L. Filion, "The electrodermal system," *Handbook Psychophysiol.*, vol. 2, pp. 200–223, 2007.

[47] O. Pabst, O. G. Martinsen, and L. Chua, "The non-linear electrical properties of human skin make it a generic memristor," *Sci. Rep.*, vol. 8, no. 1, Oct. 2018, Art. no. 15806, doi: 10.1038/s41598-018-34059-6.

[48] T. Yamamoto and Y. Yamamoto, "Non-linear electrical properties of skin in the low frequency range," *Med. Biol. Eng. Comput.*, vol. 19, no. 3, pp. 302–310, May 1981, doi: 10.1007/BF02442549.

[49] D. R. Bach, G. Flandin, K. J. Friston, and R. J. Dolan, "PsPM-SCRV10: Skin conductance responses to loud sounds, simultanously recorded from palm, fingers and foot," *Zenodo*, Feb. 2017, doi: 10.5281/zenodo.291465.

[50] J. F. Murray and K. Kreutz-Delgado, "Visual recognition and inference using dynamic overcomplete sparse learning," *Neural Comput.*, vol. 19, no. 9, pp. 2301–2352, 2007, doi: 10.1162/neco.2007.19.9.2301.

[51] R. Zdunek and A. Cichocki, "Improved M-FOCUSS algorithm with overlapping blocks for locally smooth sparse signals," *IEEE Trans. Signal Process.*, vol. 56, no. 10, pp. 4752–4761, Oct. 2008.

[52] D. L. Donoho, "De-noising by soft-thresholding," *IEEE Trans. Inf. Theory*, vol. 41, no. 3, pp. 613–627, May 1995.

[53] I. F. Gorodnitsky and B. D. Rao, "Sparse signal reconstruction from limited data using focuss: A re-weighted minimum norm algorithm," *IEEE Trans. Signal Process.*, vol. 45, no. 3, pp. 600–616, Mar. 1997.

[54] J. F. Murray, "Visual recognition, inference and coding using learned sparse overcomplete representations," Ph.D. dissertation, Univ. California, San Diego, CA, USA, 2005.

[55] G. H. Golub, M. Heath, and G. Wahba, "Generalized cross-validation as a method for choosing a good ridge parameter," *Technometrics*, vol. 21, no. 2, pp. 215–223, 1979.

[56] T. Hastie, R. Tibshirani, and J. Friedman, *The Elements of Statistical Learning: Data Mining, Inference, and Prediction*. Berlin, Germany: Springer, 2009.

[57] G. Wahba, "Smoothing noisy data with spline functions," *Numerische Mathematik*, vol. 24, no. 5, pp. 383–393, 1975.

[58] J. Torniainen, B. Cowley, A. Henelius, K. Lukander, and S. Pakarinen, "Feasibility of an electrodermal activity ring prototype as a research tool," in *Proc. IEEE 37th Annu. Int. Conf. Eng. Med. Biol. Soc.*, 2015, pp. 6433–6436.

[59] A. S. Scerbo, L. W. Freedman, A. Raine, M. E. Dawson, and P. H. Venables, "A major effect of recording site on measurement of electrodermal activity," *Psychophysiology*, vol. 29, no. 2, pp. 241–246, 1992.

[60] T. Fawcett, "An introduction to ROC analysis," *Pattern Recognit. Lett.*, vol. 27, no. 8, pp. 861–874, 2006.

[61] K. H. Zou, A. J. O'Malley, and L. Mauri, "Receiver-operating characteristic analysis for evaluating diagnostic tests and predictive models," *Circulation*, vol. 115, no. 5, pp. 654–657, 2007.

[62] D. J. Hand and R. J. Till, "A simple generalisation of the area under the ROC curve for multiple class classification problems," *Mach. Learn.*, vol. 45, pp. 171–186, 2001.